plos.org create account sign in

PLOS COMPUTATIONAL BIOLOGY

OPEN ACCESS PEER-REVIEWED

RESEARCH ARTICLE

Identifying essential factors for energy-efficient walking control across a wide range of velocities in reflex-based musculoskeletal systems

Shunsuke Koseki, Mitsuhiro Hayashibe, Dai Owaki

Published: January 19, 2024 • https://doi.org/10.1371/journal.pcbi.1011771

0 Save | 0 Citation | 1,503 View | 15 Share

Abstract
Author summary
Introduction
Generating walking through reflex-based control
Modulation of control parameters
Results
Discussion
Conclusion
Supporting information
References

Reader Comments
Figures

Subject Areas

Walking
Reflexes
Control systems
Polynomials
Legs
Hip
Knee joints
Actuators

Accessible Data

See the data

This article includes the Accessible Data icon, an experimental feature to encourage data sharing and reuse. Find out how research articles qualify for this feature.

Abstract

Humans can generate and sustain a wide range of walking velocities while optimizing their energy efficiency. Understanding the intricate mechanisms governing human walking will contribute to the engineering applications such as energy-efficient biped robots and walking assistive devices. Reflex-based control mechanisms, which generate motor patterns in response to sensory feedback, have shown promise in generating human-like walking in musculoskeletal models. However, the precise regulation of velocity remains a major challenge. This limitation makes it difficult to identify the essential reflex circuits for energy-efficient walking. To explore the reflex control mechanism and gain a better understanding of its energy-efficient maintenance mechanism, we extend the reflex-based control system to enable controlled walking velocities based on target speeds. We developed a novel performance-weighted least squares (PWLS) method to design a parameter modulator that optimizes walking efficiency while maintaining target velocity for the reflex-based bipedal system. We have successfully generated walking gaits from 0.7 to 1.6 m/s in a two-dimensional musculoskeletal model based on an input target velocity in the simulation environment. Our detailed analysis of the parameter modulator in a reflex-based system revealed two key reflex circuits that have a significant impact on energy efficiency. Furthermore, this finding was confirmed to be not influenced by setting parameters, i.e., leg length, sensory time delay, and weight coefficients in the objective cost function. These findings provide a powerful tool for exploring the neural bases of locomotion control while shedding light on the intricate mechanisms underlying human walking and hold significant potential for practical engineering applications.

Author summary

Previous reflex-based control systems face significant limitations in accurately regulating walking velocity owing to the vast number of control parameters involved. This hinders identifying essential reflex circuits that have a significant impact on energy-efficient walking across a wide range of speeds. Our research tackles this challenge by developing a reflex-based control framework that precisely regulates the velocities of the bipedal model through the performance-weighted least squares (PWLS) method that optimizes the control parameter values while considering energy efficiency. Through a detailed analysis, we identify two key reflex circuits essential for generating energy-efficient walking over a wide range of velocities. We hope that our research will inspire future investigations into reflex mechanisms and facilitate the development of advanced walking control systems for practical applications, such as gait-assisted exoskeletons and prosthetic legs, and robot control.

Figures

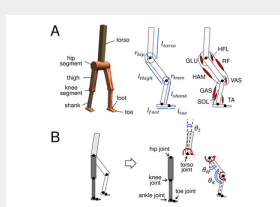

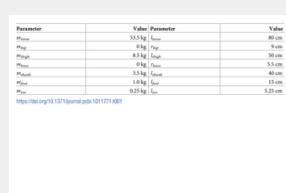

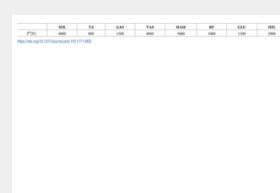

Citation: Koseki S, Hayashibe M, Owaki D (2024) Identifying essential factors for energy-efficient walking control across a wide range of velocities in reflex-based musculoskeletal systems. PLoS Comput Biol 20(1): e1011771. https://doi.org/10.1371/journal.pcbi.1011771

Editor: Jian Liu, JHU, UNITED STATES

Received: April 12, 2023; **Accepted:** December 18, 2023; **Published:** January 19, 2024

Copyright: © 2024 Koseki et al. This is an open access article distributed under the terms of the Creative Commons Attribution License, which permits unrestricted use, distribution, and reproduction in any medium, provided the original author and source are credited.

Data Availability: All experimental data and programming code are publicly available on GitHub, at https://github.com/Shunsuke-KK/reflex_plos_revision.

Funding: This work was supported by the JSPS KAKENHI Grant-in-Aid for Scientific Research on Innovative Areas Hyper-Adaptability Project (JP20H05458 and JP22H04764, M.H.) and Scientific Research (A) (JP23H00481, D.O.). The funders had no role in study design, data collection and analysis, decision to publish, or preparation of the manuscript.

Competing interests: The authors have declared that no competing interests exist.

Introduction

Walking is a fundamental mode of locomotion in our daily lives. The neurological and biochemical control mechanisms that support it comprise one of the most complex autonomous control systems in the human body [1–6]. Modeling and replicating the underlying walking mechanisms is expected to contribute to engineering applications including energy-efficient bipedal robots [7–11], gait-assisted exoskeletons [12–15], smart prosthetic legs [16, 17].

One of the most crucial aspects of human walking is the energy-efficient maintenance of our controlled velocity in the range of 1.0–1.6 m/s [18]. Central pattern generators in the central nervous system engage rhythmic neural circuits that generate basic leg movements [19–23]. Equally indispensable are reflex control mechanisms, which provide rapid adjustments to external stimuli from the sensory organs [19–21, 24], even for unexpected balance loss or unpredicted ground variations during walking, thereby maintaining velocity. Notably, humans modulate the reflex response depending on the task in locomotion [25, 26]. These findings indicate that reflex mechanisms have a crucial impact on achieving stable and energy-efficient walking.

A physical simulation is a powerful tool for exploring the neural basis of walking, a complex phenomenon generated by the interaction of versatile mechanisms [27]. Previous studies have shown that reflex-based control systems can generate human-like walking in terms of muscle activities, joint angles, and torque patterns [28–37]. Notwithstanding the great advancements thereof, these systems have difficulty regulating velocity, owing to the large number of control parameters that must be properly tuned [38], e.g., Geyer [28] used 36 control parameters to generate a steady gait in a two-dimensional musculoskeletal model. Previous studies have attempted to regulate velocities within the reflex-based control frameworks [30, 32], but their methods were limited to transitions between predetermined velocities and did not provide precise velocity controls. Furthermore, the transitions between these predetermined velocities were accomplished through the utilization of distinct control parameters designated for these transitions. Given that walking speed assumes continuous values, achieving precise control over walking speed through such means would theoretically require infinite parameters for transitions. Because “transition” differs from “control” in terms of its adaptability, it is essential to extend reflex-based systems to affect precise velocity controls while improving energy efficiency to explore reflex control mechanisms in walking. Furthermore, the development of energy-efficient control over a wide range of velocities in the reflex-based system will lead to improving the performance of the controller for exoskeletons [39, 40] and prosthetic leg [17, 41] by adjusting their control parameters according to user walking velocity.

The purpose of this study is to extend the reflex-based control system to enable controlled walking velocities based on target speeds and gain a better understanding of its modulation and energy-efficient maintenance mechanism across a wide range of walking velocities. To achieve this, we developed a novel performance-weighted least squares (PWLS) method to design a parameter modulator that coordinates a vast number of control parameters for an input target velocity while maintaining energy efficiency. In short, the reflex-based control system with the parameter modulator optimized via the PWLS successfully and energetic-efficiently maintains the desired velocity from 0.7 to 1.6 m/s in a two-dimensional musculoskeletal model. Subsequently, the detailed analysis of the parameter modulator in the reflex-based system identified two key reflex circuits affecting energy efficiency across a wide range of walking velocities. The contributions of this work include (i) extending a reflex-based control system to include velocity control, (ii) providing an adaptive polynomial regression method that uses performance indices to control performance, and (iii) identifying the key reflex circuits related to energy efficiency across a wide range of walking velocities.

Generating walking through reflex-based control

Musculoskeletal model

A two-dimensional musculoskeletal model with a height of 180 cm and weight of 80 kg was employed in this study, as illustrated in Fig 1A. Detailed parameters are listed in Table 1. The model was constructed within a MuJoCo simulation environment [42]. We employed Mujoco because of its ability to conduct simulations at a relatively low computational cost while ensuring the validity of the physical calculations. Many physics engines such as OpenSim, which is often used in biomechanics research, models contact with the ground by using a spring-damper model. This approach requires using smaller timesteps to prevent the model foot from penetrating the ground, which increases computational cost. MuJoCo introduces several formulations of the physics of contact. This allows for more efficient calculations and versatile contact behaviors. As recent studies [43, 44] have aimed to transfer OpenSim models to MuJoCo to improve computational speed and use versatile contact behaviors, MuJoCo is an acceptable physics engine with physical validity involving contact. The model consists of 12 segments: torso, hip, two thighs, two knees, two shanks, two feet, and two sets of toes, based on previous studies [28, 29]. The motions of the model are constrained to the sagittal plane. The hip and knee segments possess no mass. The model has nine internal degrees of freedom, as illustrated in Fig 1B; a torso joint, hip joints, knee joints, ankle joints, and toe joints. The spring and damper constants for all joints apart from the toe joints are set to 0 Nm/rad and 1 Nms/rad, respectively. The toe joints are set with a spring constant of 30 Nm/rad, which is consistent with [29], and a damping constant of 0 Nms/rad. The spring and damper within the joint generate a torque that is proportional to the distance from the equilibrium position and friction that is proportional to the joint's angular velocity, respectively. We set the sliding friction coefficient between the feet and the ground at a relatively high value, 2.5. Then, sliding is unlikely to happen. Fig 1A illustrates the locations of the muscle actuators that generate torque in the joints. Each leg has eight muscle actuators reflecting the gluteal (GLU), hip flexor (HFL), vasti (VAS), tibialis anterior (TA), soleus (SOL), hamstring (HAM), rectus femoris (RF), and gastrocnemius (GAS) musculature.

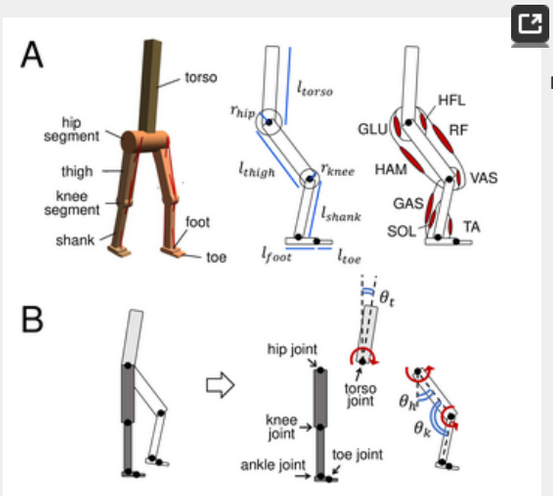

Download:

PPT PowerPoint slide

PNG larger image

TIFF original image

Fig 1. Musculoskeletal model employed in this study.
A. Structure of the musculoskeletal model. Left: Oblique view of the bipedal model in the MuJoCo simulator. Center: Side view of the model with segment parameters. Right: Muscle alignments. **B. Internal degrees of freedom of the model.** θ_t, θ_h, and θ_k represent torso joint angle, hip joint angle, and knee joint angle, respectively. The red arrows depict the positive direction of joint rotation.
https://doi.org/10.1371/journal.pcbi.1011771.g001

Parameter	Value	Parameter	Value
m_{torso}	53.5 kg	l_{torso}	80 cm
m_{hip}	0 kg	r_{hip}	9 cm
m_{thigh}	8.5 kg	l_{thigh}	50 cm
m_{knee}	0 kg	r_{knee}	5.5 cm
m_{shank}	3.5 kg	l_{shank}	40 cm
m_{foot}	1.0 kg	l_{foot}	15 cm
m_{toe}	0.25 kg	l_{toe}	5.25 cm

https://doi.org/10.1371/journal.pcbi.1011771.t001

Download:

PPT PowerPoint slide

PNG larger image

TIFF original image

Table 1. Musculoskeletal model parameters.
https://doi.org/10.1371/journal.pcbi.1011771.t001

Muscle actuator model

The musculoskeletal model includes actuators that simulate biological muscle actions that produce torque in the joints [42, 45]. The muscle actuator model comprises an inelastic tendon with a rest length of l^0 and a muscle that contracts the tendon. The muscle actuator force, F, is a function of muscle length l, velocity v, and current activation level $a \in [0, 1.0]$. A higher activation level results in a greater force being produced by the muscle. For the computation, l and v are scaled by the equilibrium length, l^0, as follows:

$$\tilde{l} = \frac{l}{l^0}, \tag{1}$$

$$\tilde{v} = \frac{v}{l^0}. \tag{2}$$

The actuator force, F, is computed as follows:

$$F(\tilde{l}, \tilde{v}, a) = \{aF_l(\tilde{l})F_v(\tilde{v}) + F_p(\tilde{l})\} \cdot F^0, \tag{3}$$

where F_l and F_v represent the force–length and force–velocity relationships, respectively. F_p represents the passive force that is always present, regardless of activation, and F^0 denotes the maximum isometric force that takes different values for each muscle actuator, as listed in Table 2. These values are consistent with those of previous studies [28, 29]. The computations of F_l, F_v, and F_p are detailed in S1 Appendix. Briefly, F_l is a function that attains a maximum value at $l = l^0$, F_v is a function that returns a smaller value for faster contraction of the muscle actuator, and F_p increases monotonically for $\tilde{l}$. The muscle current activation level, a, is calculated for the input stimulation signal, $u \in [0, 1.0]$:

$$\frac{\partial a}{\partial t} = \frac{u - a}{\tau(u, a)}, \tag{4}$$

where

$$\tau(u, a) = \begin{cases} 0.01 \cdot (0.5 + 1.5a) & (u > a) \\ 0.04/(0.5 + 1.5a) & (u \leq a) \end{cases}, \tag{5}$$

	SOL	TA	GAS	VAS	HAM	RF	GLU	HFL
F^0[N]	4000	800	1500	6000	3000	1000	1500	2000

https://doi.org/10.1371/journal.pcbi.1011771.t002

Download:

PPT PowerPoint slide

PNG larger image

TIFF original image

Table 2. Individual F^0.
https://doi.org/10.1371/journal.pcbi.1011771.t002

Reflex-based control

The reflex-based controller employed in this study is identical in principle to that of Wang et al [29]. This controller is based on the Geyer model and incorporates additional control laws to adjust the target hip joint angle and to fix the hip and knee joints prepared for the heel strike. Consequently, it more robustly produces gaits and can manage non-steady states during transitions in walking velocities. Moreover, the extended model can maintain the biomechanical explanatory ability essential to discussing gait adaptation mechanisms, which may be lost through simplification. We did not make any ad-hoc adjustments to the basic reflex-based control model to ensure optimal simulation performance. The controller computes the muscle stimulation, denoted as u_i, for each muscle, i, by incorporating sensory feedback with a time delay of Δt as input. The control law switches depending on whether the leg is in the stance or swing phase. Moreover, additional stimulation is introduced during the late stance and late swing phases. The control system comprises three primary functions: force feedback, length feedback, and muscle-driven proportional derivative (PD) control.

- Force feedback:
  The force feedback law returns the stimulation signal, u_i^F, in response to the actuator force, F_i. In humans, the signals of the F_i arise from Golgi tendon organs and are carried by type Ib afferents to the spinal cord. u_i^F is calculated as follows:

$$u_i^F = G_i \tilde{F}_i(t - \Delta t_i), \tag{6}$$

$$\tilde{F}_i(t - \Delta t_i) = \frac{F_i(t - \Delta t_i)}{F_i^0}, \tag{7}$$

  where the gain, G_i, is the positive control parameter, and $\tilde{F}_i(t - \Delta t_i)$ is the scaled actuator force, (i.e., $\tilde{F}_i = F_i/F_i^0$), which includes the sensory time delay, Δt_i.

- Length feedback
  Through length feedback, we calculate the stimulation signal, denoted as u_i^l, corresponding to the length of the muscle actuator, l_i. This function models the stretch reflex of the muscle spindle. u_i^l is calculated as follows:

$$u_i^l = \max\{0, G_i(l_i(t - \Delta t_i) - l_i^{tar})\}, \tag{8}$$

  where the target length, l_i^{tar}, and gain, G_i, are positive control parameters.

- Muscle-driven PD control
  The muscle-driven PD control generates the stimulation necessary to move joint θ_j (Fig 1B) to the target angle, θ_j^{tar}. This function can be interpreted as a polysynaptic reflex that is mediated by the joint position afferent input from group III fibers and descending signals of the target joint angles from the supraspinal. The muscle-driven PD control laws are employed to stabilize the generated gait by the hip muscles during the stance phase to balance the torso and during stance preparation to prepare for ground contact (described in S1 Appendix). For muscle actuator, i, which applies torque to joint θ_j in the positive direction, $u_i^{\theta_j}$ is defined as follows:

$$u_i^{\theta_j} = \max\{0, K_i(\theta_j^{tar} - \theta_j(t - \Delta t_i)) - D_i\dot{\theta}_j(t - \Delta t_i)\}.$$

(9)

Conversely, for muscle actuator i, which applies torque in the negative direction, u_i^{θ} is defined as follows:

$$u_i^{\theta} = \max\{0, K_i(\theta_j(t-\Delta t_i) - \theta_j^{tar}) + D_i\dot{\theta}_j(t-\Delta t_i)\}, \tag{10}$$

where the proportional gain, K_i, and derivative gain, D_i, are positive control parameters.

Fig 2 illustrates the reflexes in the stance phase and swing phase. Please see S1 Appendix or the original paper [29] for more details.

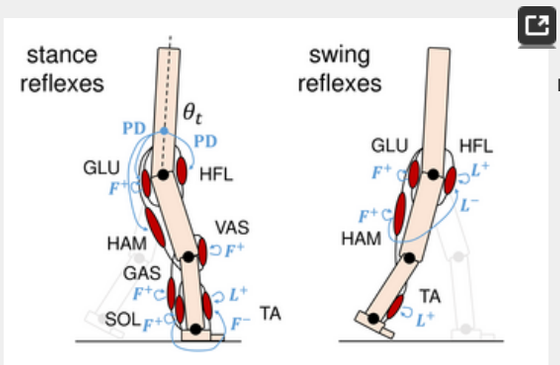

Download:

PPT PowerPoint slide

PNG larger image

TIFF original image

Fig 2. Key reflexes in the stance and swing phase.
F represents force feedback, *L* represents length feedback, and PD represents muscle-driven PD control. + and − denote positive and negative feedback, respectively. In the stance phase, F^+ at GLU, VAS, and SOL generate compliant leg behavior. L^+ at TA prevents overextension of the ankle joint, which is suppressed by the F^- from the SOL. F^+ at GAS contributes to push-off and prevents overextension of the knee joint. Muscle-driven PD controls at HFL, GLU, and HAM balance the torso. In the swing phase, L^+ facilitates leg swing, which is suppressed by L^- from HAM. F^+ at GLU and HAM apply braking force to the swing leg. L^+ at TA raises the toes to create clearance between the feet and the ground.
https://doi.org/10.1371/journal.pcbi.1011771.g002

Modulation of control parameters

Fig 3 displays the control diagram of the musculoskeletal model, which is structured into spinal and supraspinal layers. We added a parameter modulator that allows a wide range of walking while maintaining energy efficiency to the previous model [29]. The reflex-based controller in the spinal layer activates muscles. The parameter modulator in the supraspinal layer coordinates the control parameter set $\boldsymbol{Y}^{tar}$ to achieve the input target velocity, v_{vel}^{tar}. Each control parameter, $y_i^{tar} \in \boldsymbol{Y}^{tar}$, is calculated using the function $P_i(v_x)$ in the parameter modulator for the input target velocity, v_x^{tar} (Fig 4). $P_i(v_x)$ is derived via the polynomial regression of the relationship between the velocity and parameter value, which is collected using optimization by incrementally increasing/decreasing the target velocity. SIMBICON in the supraspinal cord adjusts the desired foot placements.

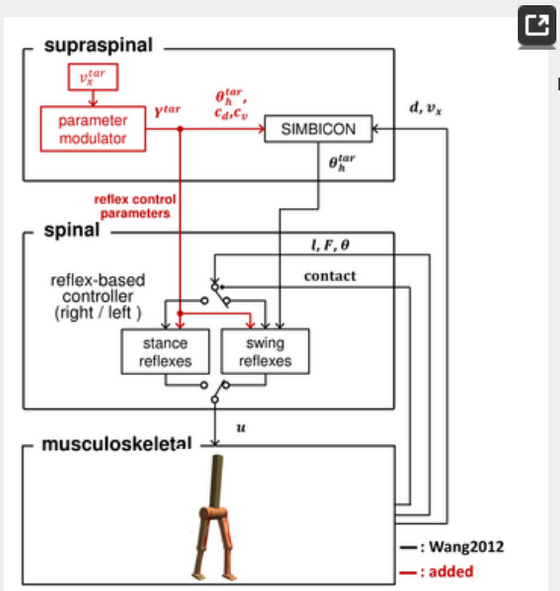

Download:

PPT PowerPoint slide

PNG larger image

TIFF original image

Fig 3. Control diagram for the musculoskeletal model.
The musculoskeletal model is driven by activated muscles receiving stimulation signals, *u*, from the reflex-based controller in the spinal layer. Each leg (right and left) is controlled by separate stance and swing reflexes. The control law switches depending on whether the leg is in contact with the ground. Sensory information from the model is fed back to the controller for motion generation. The supraspinal layer controls the walking velocity and adjusts the desired foot placements. The parameter modulator coordinates the control parameter set $\boldsymbol{Y}^{tar}$ to achieve input target velocity, v_{vel}^{tar}. SIMBICON adjusts the target hip angle, θ_h^{tar}, in the stance preparation phase using the sensory information (d and v_x, see S1 Appendix).
https://doi.org/10.1371/journal.pcbi.1011771.g003

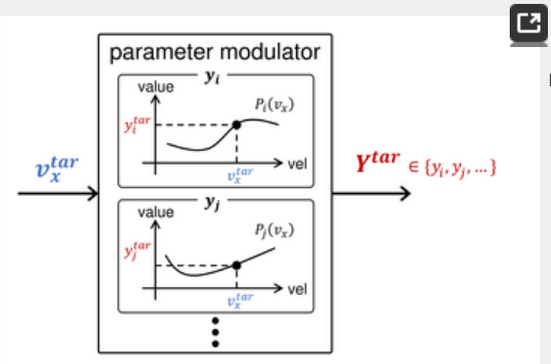

Download:

PPT PowerPoint slide

PNG larger image

TIFF original image

Fig 4. Parameter modulator.
This is located in the supraspinal layer of the controller (Fig 3). By using the polynomial function, P_i, each control parameter, y_i, is adjusted to achieve the input target velocity, v_x^{tar}.
https://doi.org/10.1371/journal.pcbi.1011771.g004

Optimizing control parameters

The dataset for polynomial regression is collected via optimization by incrementally changing the target velocity. In total, there are 56 control parameters, $\boldsymbol{Y} \in \mathbb{R}^{56}$. Details are provided in S1 Appendix. We optimize these parameters using the covariance matrix adaptation evolution strategy (CMA-ES) algorithm [46], which is well-suited for nonlinear and non-convex optimization problems. In this algorithm, independent λ search points are sampled from a multivariate normal distribution, $\mathcal{N}$, at each generation, g:

$$\boldsymbol{Y}^{(g+1)} \sim \mathcal{N}(\boldsymbol{m}^{(g)}, \sigma^{(g)^2}\boldsymbol{C}^{(g)}), \tag{11}$$

where $\boldsymbol{Y}$ represents the reflex control parameter set in this study, $\boldsymbol{m}^{(g)}$ represents the mean value of the search distribution at generation g, $\sigma^{(g)}$ represents the step size at generation g, and $\boldsymbol{C}^{(g)}$ represents the covariance matrix at generation g. The sampled control parameter set, $\boldsymbol{Y}$, is evaluated using the objective function, f. Then, using the top μ data points from λ offspring along with the evolution paths, $p_\sigma^{(g)}$ and $p_C^{(g)}$, which accumulate historical search directions, $\boldsymbol{m}$, σ, $\boldsymbol{C}$, p_σ, and p_C are updated.

The evaluation of $\boldsymbol{Y}$ is conducted from a fixed initial state until time step T', in which the musculoskeletal model falls, with an upper limit T. More specifically, if the model falls before reaching an upper time step T, the evaluation is terminated at that time step T', and else $T' = T$. We judge that the model has fallen when any segment above the knee comes into contact with the ground. By terminating the unnecessary evaluations prior to reaching the maximum time step, the computation time can be reduced. Optimization is conducted to determine the optimal solution that minimizes the objective cost function. To generate an energy-efficient gait that follows the target velocity, the objective cost function, f, is designed as follows based on previous studies [29, 30]:

$$f(\boldsymbol{Y}) = \sum_{t=1}^{T'} r(\boldsymbol{s}_t) + \alpha_E(\mathrm{CoT} - 0.3), \tag{12}$$

where $\boldsymbol{s}_t$ represents the state of the model at time step t as determined by the control parameter set, $\boldsymbol{Y}$, r represents the reward function for state $\boldsymbol{s}_t$, α_E represents the weight coefficient, and CoT represents the cost of transport [47]. Reward function r is defined as follows:

$$r(\boldsymbol{s}_t) = r_{alive} + r_{forward} + r_{torso} + r_{fall}, \tag{13}$$

$$r_{alive} = -1, \tag{14}$$

$$r_{forward} = \min(1, \alpha_v|v_x - v_x^{tar}|^2), \tag{15}$$

$$r_{torso} = \alpha_t\theta_t^2, \tag{16}$$

$$r_{fall} = \begin{cases} 0 \\ 5,000 & (\text{fall down} \wedge T' \leq 700) \end{cases}, \tag{17}$$

where r_{alive} prevents the model from falling. If the model does not fall over long timesteps, this term can reduce the total cost. $r_{forward}$ represents the penalty for the difference between the current horizontal walking speed, v_x, and the target velocity, v_x^{tar}, with a lower limit of -1. r_{torso} is established to maintain an upright torso. r_{fall} incurs a large cost if the model falls within 700 timesteps of the initial state. This prevents convergences at local minima, where the model falls forward immediately from the initial position at the target velocity. α_E(CoT − 0.3) in f represents the energy cost added at the end of a trial. 0.3 is the deviation, which in turn permits a larger weight coefficient on CoT. The CoT quantifies the energy efficiency of locomotion, and a lower value indicates better energy efficiency [47]. The CoT is expressed by the following equation:

$$\mathrm{CoT} = \frac{J}{Mg\Delta d}, \tag{18}$$

where J represents the total metabolic energy, M represents the model mass, g represents the acceleration of gravity, and Δd represents the distance traveled. J is calculated by summing the total metabolic energy expended by all muscles, as described in previous studies [29, 48]. The detailed equations for J are provided in S1 Appendix.

Dataset collection for polynomial regression

We run two programs in parallel to collect the data efficiently. Within one thread, initially, the target velocity, v_x^{tar}, in cost function f (Eq (12)) is set to 1.3 m/s, which is the human self-selected speed [29]. Control parameter set, $\boldsymbol{Y}$, that generate a gait around v_x^{tar} are obtained. Then, v_x^{tar} is slightly increased to $v_x^{tar} + \Delta v_x$, and the corresponding control parameter set around the updated target velocity are collected. This process is repeated until v_x^{tar} reaches the upper limit of the target velocity, $v_{x\,max}^{tar}$ (See S1 Appendix in detail). Within the other thread, the target velocity, v_x^{tar} is initially set to 1.2 m/s. Then, v_x^{tar} is slightly decreased to $v_x^{tar} - \Delta v_x$ and this process is also repeated until v_x^{tar} reaches the lower limit of the target velocity, $v_{x\,min}^{tar}$. The initial control parameters are set identically in both programs.

The control parameters, $\boldsymbol{Y}$, are optimized using the G generation for each target velocity, v_x^{tar}. When v_x^{tar} is changed, σ in Eq (11) is reset to σ^0 and p_σ, and the p_C are emptied, whereas $\boldsymbol{m}$ and $\boldsymbol{C}$ are maintained. If model-walking is maintained at the upper timestep limit of the evaluation trial with control parameters $\boldsymbol{Y}$, a tuple consisting of walking speed, control parameters, and CoT $\{(v_x, \boldsymbol{Y}, \mathrm{CoT})\}$ is added to the dataset. Notably, the dataset with n data points, $\{(v_{x1}, \boldsymbol{Y}_1, \mathrm{CoT}_1), \ldots, (v_{xn}, \boldsymbol{Y}_n, \mathrm{CoT}_n)\}$, is sorted according to velocity v_x (i.e., $v_{x1} \le v_{x2} \le \ldots \le v_{xn}$).

PWLS (Performance Weighted Least Square method)

Each control parameter, $y_i^{tar} \in \boldsymbol{Y}^{tar}$, is modulated through an mth degree polynomial function, $P_i(v_x)$ (Fig 4), for the input velocity, v_x, as follows:

$$y_i = P_i(v_x), \tag{19}$$

$$= \omega_{i0} v_x^0 + \omega_{i1} v_x^1 + \ldots + \omega_{im} v_x^m, \tag{20}$$

where ω_{ij} are coefficients calculated using our proposed PWLS, a polynomial regression algorithm that minimizes the total squared performance-weighted error of data points. Unlike the normal least-squares method in which data points are treated without bias when calculating the total squared error, PWLS derives the polynomial function from dataset with bias. Thus, it assigns a greater weight to higher-performing data points to reinforce energy-efficient walking via regression. PWLS is similar to the weighted least-squares method [49]. The weighted least square method is the polynomial regression algorithm that is used when handling heteroscedastic data, meaning that the variance among the measured points is not constant. The variables that cause the variance of observations are incorporated to weigh each data point. In our PWLS, each data point is weighted according to its performance instead of the factor that causes heteroscedastic.

Suppose there are n data points, $\{(v_{x1}, y_{i1}), \ldots, (v_{xn}, y_{in})\}$, for each control parameter from the collected dataset, $\{(v_{x1}, \boldsymbol{Y}_1, \mathrm{CoT}_1), \ldots, (v_{xn}, \boldsymbol{Y}_n, \mathrm{CoT}_n)\}$. The total error between y_i and the expected value derived from P_i can be expressed in matrix form as

$$\| \boldsymbol{y_i} - \boldsymbol{V\omega_i} \|_2 = \left\| \begin{bmatrix} y_{i\,1} \\ y_{i\,2} \\ \vdots \\ y_{i\,n} \end{bmatrix} - \begin{bmatrix} v_{x_1}^0 & v_{x_1}^1 & \ldots & v_{x_1}^m \\ v_{x_2}^0 & v_{x_2}^1 & \ldots & v_{x_2}^m \\ \vdots & \vdots & \ddots & \vdots \\ v_{x_n}^1 & v_{x_n}^1 & \ldots & v_{x_n}^m \end{bmatrix} \begin{bmatrix} \omega_{i0} \\ \omega_{i1} \\ \vdots \\ \omega_{im} \end{bmatrix} \right\|_2, \tag{21}$$

where $\|\cdot\|_2$ represents Euclidean norm and

$$\boldsymbol{y_i} = \begin{bmatrix} y_{i\,1} \\ y_{i\,2} \\ \vdots \\ y_{i\,n} \end{bmatrix} \in \mathbb{R}^n, \tag{22}$$

$$\boldsymbol{V} = \begin{bmatrix} v_{x_1}^0 & v_{x_1}^1 & \dots & v_{x_1}^m \\ v_{x_2}^0 & v_{x_2}^1 & \dots & v_{x_2}^m \\ \vdots & \vdots & \ddots & \vdots \\ v_{x_n}^1 & v_{x_n}^1 & \dots & v_{x_n}^m \end{bmatrix} \in \mathbb{R}^{n\times(m+1)}, \tag{23}$$

$$\boldsymbol{\omega_i} = \begin{bmatrix} \omega_{i\,0} \\ \omega_{i\,1} \\ \vdots \\ \omega_{i\,m} \end{bmatrix} \in \mathbb{R}^{m+1}. \tag{24}$$

Subsequently, each error is weighted by $\boldsymbol{\beta} = [\beta_1, \dots .\beta_n]^{\mathrm{T}} \in \mathbb{R}^n$, where β_i represents the evaluated performance value of the corresponding data point, *i*, with higher values indicating more favorable data. We define the following total performance-weighted error:

$$\| \boldsymbol{\beta} \otimes (\boldsymbol{y_i} - \boldsymbol{V\omega_i}) \|_2, \tag{25}$$

where ⊗ denotes the Hadamard product, which takes two matrices of the same size and returns a matrix in which each element is the product of the original elements (see S1 Appendix).

In PWLS, the ω_{ij} coefficients are determined so that they minimize the total performance-weighted squared error, E_{PWLS}. Given that the error for each data point is weighted by its evaluated performance, β_i, the errors are more suppressed for high-performing data points and permissible for low-performing data points. E_{PWLS} is the square of Eq (25),

$$E_{PWLS} = \| \boldsymbol{\beta} \otimes (\boldsymbol{y_i} - \boldsymbol{V\omega_i}) \|_2^2, \tag{26}$$

$$= (\boldsymbol{\beta} \otimes (\boldsymbol{y_i} - \boldsymbol{V\omega_i}))^{\mathrm{T}} (\boldsymbol{\beta} \otimes (\boldsymbol{y_i} - \boldsymbol{V\omega_i})). \tag{27}$$

The partial derivative of E_{PWLS} with respect to $\boldsymbol{\omega_i}$ is given by

$$\frac{\partial E_{PWLS}}{\partial \boldsymbol{\omega_i}} = 2(\boldsymbol{\beta} \otimes (\boldsymbol{y_i} - \boldsymbol{V\omega_i}))^{\mathrm{T}} \frac{(\boldsymbol{\beta} \otimes (\boldsymbol{y_i} - \boldsymbol{V\omega_i}))}{\partial \boldsymbol{\omega_i}}, \tag{28}$$

$$= 2(\boldsymbol{\beta} \otimes (\boldsymbol{y_i} - \boldsymbol{V\omega_i}))^{\mathrm{T}} (-\boldsymbol{B} \otimes \boldsymbol{V}), \tag{29}$$

where $\boldsymbol{B}$ is an $n \times (m + 1)$ matrix that expands $\boldsymbol{\beta}$ along the horizontal axis and is defined as follows:

$$\boldsymbol{B} = \begin{bmatrix} \beta_1 & \beta_1 & \dots & \beta_1 \\ \beta_2 & \beta_2 & \dots & \beta_2 \\ \vdots & \vdots & \ddots & \vdots \\ \beta_n & \beta_n & \dots & \beta_n \end{bmatrix} \in \mathbb{R}^{n\times(m+1)}. \tag{30}$$

E_{PWLS} attains its minimum value when

$$\frac{\partial E_{PWLS}}{\partial \boldsymbol{\omega_i}} = 0. \tag{31}$$

Thus, the objective of PWLS is to solve Eq (31) with respect to $\boldsymbol{\omega_i}$. Combining Eqs (29) and (31) yields

$$2(\boldsymbol{\beta} \otimes (\boldsymbol{y_i} - \boldsymbol{V\omega_i}))^{\mathrm{T}} (-\boldsymbol{B} \otimes \boldsymbol{V}) = 0, \tag{32}$$

$$(\boldsymbol{\beta} \otimes (\boldsymbol{y_i} - \boldsymbol{V\omega_i}))^{\mathrm{T}} (\boldsymbol{B} \otimes \boldsymbol{V}) = 0. \tag{33}$$

Using the property, $(\boldsymbol{U}\,\boldsymbol{V})^T = \boldsymbol{V}^T\boldsymbol{U}^T$, Eq (33) can be rewritten as

$$(\boldsymbol{B} \otimes \boldsymbol{V})^{\mathrm{T}} (\boldsymbol{\beta} \otimes (\boldsymbol{y_i} - \boldsymbol{V\omega_i})) = 0, \tag{34}$$

$$(\boldsymbol{B} \otimes \boldsymbol{V})^{\mathrm{T}} (\boldsymbol{\beta} \otimes \boldsymbol{y_i}) - (\boldsymbol{B} \otimes \boldsymbol{V})^{\mathrm{T}} (\boldsymbol{\beta} \otimes \boldsymbol{V\omega_i}) = 0, \tag{35}$$

$$(\boldsymbol{B} \otimes \boldsymbol{V})^{\mathrm{T}} (\boldsymbol{\beta} \otimes \boldsymbol{V\omega_i}) = (\boldsymbol{B} \otimes \boldsymbol{V})^{\mathrm{T}} (\boldsymbol{\beta} \otimes \boldsymbol{y_i}).$$

(36)

Here, $\boldsymbol{\beta} \otimes \boldsymbol{V}\,\boldsymbol{\omega_i}$ in Eq (36) can be reformulated (see S1 Appendix) as follows:

$$\boldsymbol{\beta} \otimes \boldsymbol{V}\boldsymbol{\omega_i} = (\boldsymbol{B} \otimes \boldsymbol{V})\boldsymbol{\omega_i}. \tag{37}$$

By substituting Eq (37) into Eq (36), we obtain

$$(\boldsymbol{B} \otimes \boldsymbol{V})^{\mathrm{T}}(\boldsymbol{B} \otimes \boldsymbol{V})\boldsymbol{\omega_i} = (\boldsymbol{B} \otimes \boldsymbol{V})^{\mathrm{T}}(\boldsymbol{\beta} \otimes \boldsymbol{y_i}). \tag{38}$$

Consequently, the polynomial coefficient, $\boldsymbol{\omega_i}$, in P_i can be computed as follows:

$$\boldsymbol{\omega_i} = ((\boldsymbol{B} \otimes \boldsymbol{V})^{\mathrm{T}}(\boldsymbol{B} \otimes \boldsymbol{V}))^{-1}(\boldsymbol{B} \otimes \boldsymbol{V})^{\mathrm{T}}(\boldsymbol{\beta} \otimes \boldsymbol{y_i}). \tag{39}$$

Design of weight parameters $\boldsymbol{\beta}$

$\beta_i \in \boldsymbol{\beta}$ is the performance evaluated in the PWLS to weigh corresponding data i. In this study, we evaluate the performance of each data point in terms of energy efficiency using the CoT. We design β such that it has a higher value when the CoT is low. Because the energy consumed in human walking depends on speed [50], it is unreasonable to compare CoT values between data with widely different speeds. Thus, we calculate β relative to the average CoT measured around the generated walking speed. Because the dataset, $\{(v_{x1}, \boldsymbol{Y}_1, \mathrm{CoT}_1), \ldots, (v_{xi}, \boldsymbol{Y}_i, \mathrm{CoT}_i), \ldots, (v_{xn}, \boldsymbol{Y}_n, \mathrm{CoT}_n)\}$, is sorted by speed, the average CoT around the jth data point, $\overline{\mathrm{CoT}}_j$, is calculated as follows:

$$\overline{\mathrm{CoT}}_j = \frac{\mathrm{CoT}_{j-M} + \mathrm{CoT}_{j-M+1} + \ldots + \mathrm{CoT}_{j+M}}{2M+1}. \tag{40}$$

In this study, M was set to 125, giving $2M + 1 = 251$, which is approximately 0.5% of the control parameter sets collected in the dataset. Using the average CoT value around the ith data point, $\overline{\mathrm{CoT}}_i$, we defined the weight for data i, β_i, as follows:

$$\beta_j = A\left(\frac{\overline{\mathrm{CoT}}_j - \mathrm{CoT}_j}{\overline{\mathrm{CoT}}_j}\right), \tag{41}$$

where $A \geq 1$ denotes a constant. $\beta_i > 1$ indicates that the data are evaluated as favorable data and $\beta_i < 1$ as unfavorable data. For example, when $\mathrm{CoT}_i < \overline{\mathrm{CoT}}_i$ (i.e., generated gait was more energy-efficient), $\left(1 - \frac{\mathrm{CoT}_i}{\overline{\mathrm{CoT}}_j}\right)$ is calculated above 0, and this yielded $\beta_i > 1$. A smaller CoTi value in comparison to the average CoT value, $\overline{\mathrm{CoT}}_i$, results in the exponential increase of β_i based on the A value. Therefore, the parameter A determines the strength of the bias toward higher-performing data points, i.e., a larger A value indicates a greater bias toward favorable data.

Simple application example of PWLS

In this section, we explain how PWLS computes polynomials, based on a simple illustrative example. We assume that there is a dataset of a control parameter y_i, comprising a total of 18 × 9 data points, each evaluated through the CoT as depicted in Fig 5. The horizontal axis indicates the generated walking velocity and the vertical axis indicates the control parameter value. The black-colored data points correspond to a lower CoT value of 0.5 (more efficient), while the grey-colored data points correspond to a higher CoT value of 1.0 (less efficient). Fig 5 illustrates polynomials calculated through PWLS. It can be found that the polynomials pass close to the data points with highly evaluated data points with larger A, which determines the strength of the bias toward highly- evaluated data points (Eq (41)). Thus, by assigning a greater weight to higher-performing data points, walking energy efficiency can be reinforced via regression.

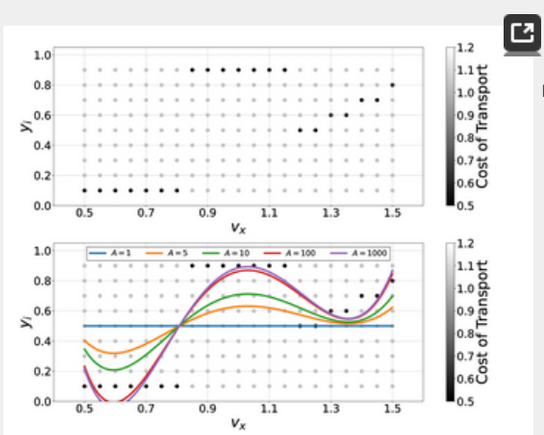

Download:

PPT PowerPoint slide

PNG larger image

TIFF original image

Fig 5. The regression curve derived through PWLS with different *A* values.
Upper: The prepared dataset comprises 18 × 9 data points, each is evaluated through the CoT. The black-colored data points represent a lower CoT value of 0.5 (efficient), while the gray-colored data points represent a higher CoT value of 1.0 (inefficient). Lower: Calculated regression curves, with a polynomial degree set to 6.
https://doi.org/10.1371/journal.pcbi.1011771.g005

Results

In the optimization, the upper timestep for each evaluation trial was set to T = 5, 000 steps (25 s). The weight coefficients in the objective cost function, f, were set as α_E = 5000, α_v = 5 and α_t = 1.0. We collected the dataset by running two programs in parallel with v_x^{tar} incrementally increase/decrease in 0.1 m/s intervals. Within one thread, v_x^{tar} was initially set to 1.3 m/s and increased to $v_{x\,max}^{tar} = 2.0$ m/s. Within the other thread, v_x^{tar} was initially set to 1.2 m/s and decreased to $v_{x\,min}^{tar} = 0.4$ m/s. For each v_x^{tar}, λ = 20 points were sampled per generation, with a generation number of G = 300, which we confirmed that optimization was converged (See S1 Appendix). This resulted in 102,000 evaluation trials. The other hyperparameters for CMA-ES were set to σ^0 = 0.1 and μ = 7. λ and μ are recommended value [46]. σ^0 was set to be large, but not out of the solution space in the optimization process. Data collection required approximately three days on a Lenovo ThinkPad E470 20H2S04L00. Out of all trials, we added approximately 50% to the dataset. Fig 6 illustrates the generated walking speeds and the CoTs in a dataset, indicating a concave quadratic relationship similar to human walking [50]. Using PWLS, we obtained P_i (Fig 4). We found that at least a polynomial degree of m = 6 is required to generate gaits. Therefore, to compute polynomials with minimal computational cost and to avoid overfitting, we chose a polynomial degree of m = 6.

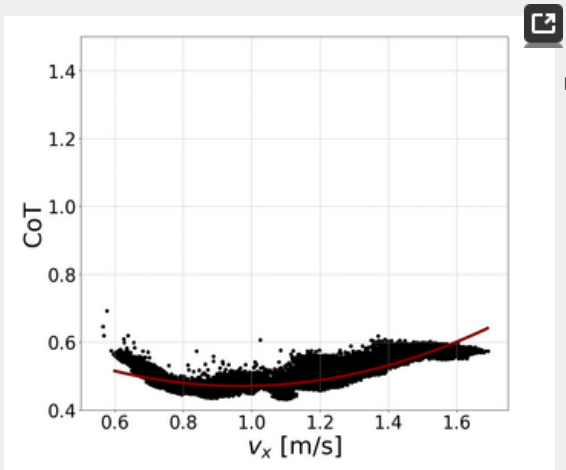

Download:

PPT PowerPoint slide

PNG larger image

TIFF original image

Fig 6. Generated walking speeds and their CoTs in the dataset.
The CoT velocity value can be approximated by quadratic curves (red lines).
https://doi.org/10.1371/journal.pcbi.1011771.g006

Generated gaits

To stabilize walking before setting v^{tar}, we controlled the musculoskeletal model with parameters that produced a stable gait at 1.25 m/s for a distance of 2.0 m from the initial position. We found that steady walking was generated for $v_x^{tar} = 0.75 - 1.6\,\mathrm{m/s}$ by using the optimized functions derived with A = 1 − 10^6 in Eq (41) (see S1 Video). Here, We defined steady walking as being able to walk more than 30 m without falling. The actual speeds were approximately to v_x^{tar} (see S1 Appendix). Fig 7 displays snapshots of the generated gaits for v_x^{tar} at 0.9 (slow), 1.25 (normal), and 1.6 (fast) m/s.

Download:

PPT PowerPoint slide

PNG larger image

TIFF original image

Fig 7. Snapshots of the generated gait.
We captured data every 0.25 s for v_x^{tar} at 0.9, 1.25, and 1.6 m/s. See S1 Video.
https://doi.org/10.1371/journal.pcbi.1011771.g007

Fig 8 illustrates the ground reaction forces (GRF) and kinematics of the generated gait using the optimized functions derived with A = 10^6 and those of humans at corresponding speeds [51]. Although undershoots and overshoots were observed, the cross-correlation values (R) between the GRF of the generated and human gaits were consistently positive. In kinematics, the cross-correlation values for hip and knee joints were close to 1, whereas the value for the ankle joint was nearly 0.

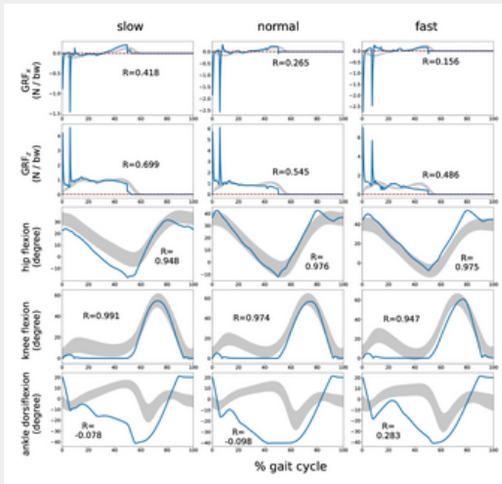

Download:

PPT PowerPoint slide

PNG larger image

TIFF original image

Fig 8. GRFs and kinematics of the generated gait.
v_x^{tar} was set to 0.9 (slow), 1.25 (normal), and 1.6 m/s (fast). Blue lines depict the generated gait, while gray lines represent those of humans (mean±1 s.d.) [51]. GRFs values are normalized by the body weight. *R* denotes the cross-correlation value.
https://doi.org/10.1371/journal.pcbi.1011771.g008

Velocity control

In this section, we demonstrate the velocity control ability of the designed reflex-based controller. The upper graph in Fig 9 illustrates the velocity of the model with a change in v_x^{tar} (dotted line) between the minimum and maximum values. The bottom graph in Fig 9 indicates an additional experimental result in which v_x^{tar} was changed from 1.2 to 0.8 to 1.0 to 1.5, and finally to 1.3 m/s. In all cases, the rate of change of v_x^{tar} was set to 0.05/s. As illustrated in the figures, the model regulates the velocities based on the target velocity.

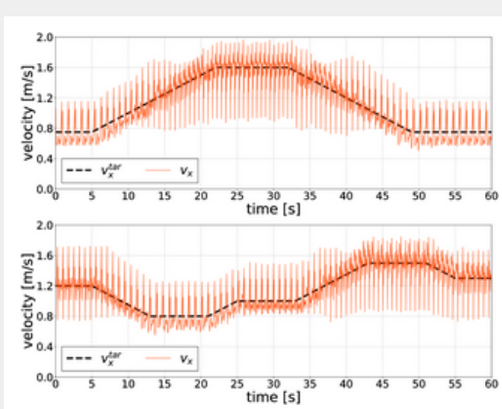

Download:

PPT PowerPoint slide

PNG larger image

TIFF original image

Fig 9. The regression curve derived through PWLS with different *A* values.
Upper: The prepared dataset comprises 18 × 9 data points, each is evaluated through the CoT. The black-colored data points represent a lower CoT value of 0.5 (efficient), while the gray-colored data points represent a higher CoT value of 1.0 (inefficient). Lower: Calculated regression curves, with a polynomial degree set to 6.
https://doi.org/10.1371/journal.pcbi.1011771.g009

Performance evaluation of PWLS

In this section, we evaluate the optimization performance of the proposed polynomial regression (PWLS) method. PWLS calculates regression curves by weighting higher-performing (i.e., energy-efficient) data points, in which *A* determines the strength of the bias toward them. Fig 10 left shows the estimated CoT curves for the generated walking with different *A* values (A = 1, 10, 10^2, 10^4, and 10^6) in Eq (41). To quantify the performance of the PWLS, we defined the integrated CoT value over the corresponding velocity range, ∫CoT, as follows:

$$\int \mathrm{CoT} = \int_{v_{x\,min}}^{v_{x\,max}} \mathrm{CoT}\, dv_x, \tag{42}$$

where v_{xmin} and v_{xmax} represent the lower and upper limits of the velocity that the model can walk. For example, when the model can walk from v_{xmin} = 0.7 m/s to v_{xmax} = 1.6 m/s and the estimated CoT curve is represented $\mathrm{CoT} = 0.6v_x^2 - 1.2v_x - 0.1$, ∫CoT is calculated as follows:

$$\int \mathrm{CoT} = \int_{v_{x\,min}=0.7\,\mathrm{m/s}}^{v_{x\,max}=1.6\,\mathrm{m/s}} (0.6v_x^2 - 1.2v_x - 0.1)\, dv_x \simeq 0.556. \tag{43}$$

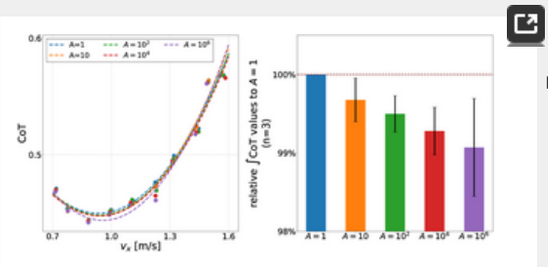

Download:

PPT PowerPoint slide

PNG larger image

TIFF original image

Fig 10. Contribution of the PWLS to gait generation.
Left: Estimated CoT curves for generated gaits with different *A* values. Right: Relative ∫CoT value of the generated gaits with different *A* values (n = 3). The generated gait with $A = 1$ is the baseline. ∫CoT is the integral of the estimated CoT curves from the lower limit velocity (=0.7 m/s) to the upper limit velocity (=1.6 m/s).
https://doi.org/10.1371/journal.pcbi.1011771.g010

Fig 10 right presents relative ∫CoT value of the generated gaits with different *A* values. Regardless of the *A* value, v_{xmin} (=0.6 m/s) and v_{xmax} (=1.6 m/s) were set to be identical. We found that lower ∫CoT for larger *A*: more energy-efficient walking was generated with larger *A*. However, excessive *A* resulted in increased instability: we could not find steady walking at specific v_x^{tar} values for $A > 10^8$.

Identifying factors essential for improving energy efficiency

In this study, we aim to identify the key reflex circuits that influence energy-efficient walking across a wide range of velocities. First, to identify the essential factors for improved energy efficiency, we substituted the optimized function of each control parameter that derived at $A = 10^6$, which achieved more energy-efficient walking over a wide range of velocities, in the gait with $A = 1$. Fig 11 illustrates this approach. Fig 12 illustrates the absolute change in percentage of the ∫CoT values, Δ|∫CoT|, to the generated gait with $A = 1$. From the results, we found that G_{HFL}, l_{HAM}^{tar} and θ_t^{tar} are the three parameters that changed Δ|∫CoT| value by more than 0.5%. This result suggests that reflex circuits that involve these parameters may have a significant impact on energy-efficient walking across a wide range of velocities. The two length-feedback reflex circuits, $G_{HFL}(l_{HFL} - l_{HFL}^{tar})$ and $G_{HAM_HFL}(l_{HAM} - l_{HAM_HFL}^{tar})$, is the primary circuits involved in these parameters, G_{HFL} and l_{HAM}^{tar}: both reflex circuits stimulate HFL muscle during the swing phase (Fig 13). θ_t^{tar}, which is the reference angle of the torso, changed Δ|∫CoT| value of the third. This parameter was not related to a specific reflex circuit but was shared with several reflex circuits.

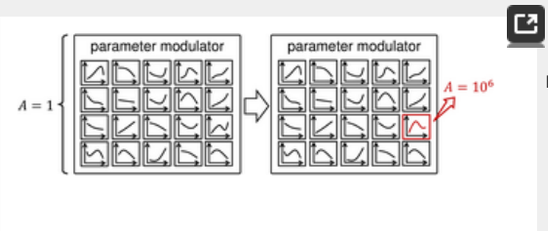

Download:

PPT PowerPoint slide

PNG larger image

TIFF original image

Fig 11. Illustration of the replacement of the optimized function.
Left: Before the replacement, all functions were derived with $A = 1$. Right: Only the target control parameter function (red) was replaced with $A = 10^6$. Functions with other parameters were not replaced.
https://doi.org/10.1371/journal.pcbi.1011771.g011

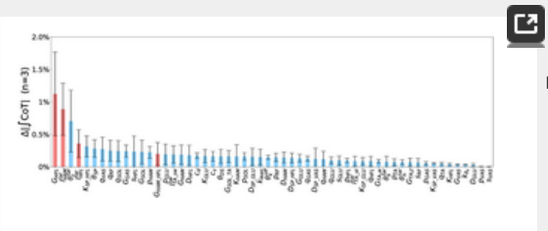

Download:

PPT PowerPoint slide

PNG larger image

TIFF original image

Fig 12. Absolute change in ∫CoT values when the optimized function of each parameter was substituted to that derived with $A = 10^6$ in the generated gait with $A = 1$ ($n = 3$).
The red bars represent control parameters associated with the reflex circuits under focus.
https://doi.org/10.1371/journal.pcbi.1011771.g012

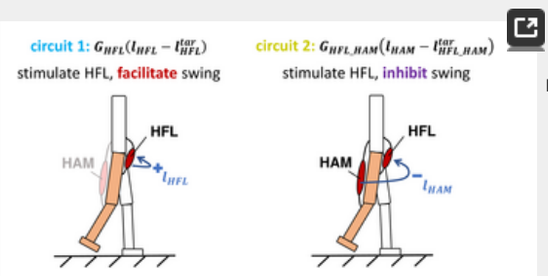

Download:

PPT PowerPoint slide

PNG larger image

TIFF original image

Fig 13. Key reflex circuits for energy-efficient gait.
$G_{HFL}(l_{HFL} - l^{tar}_{HFL})$ is the positive length feedback stimulating HFL to swing the leg forward. $G_{HAM_HFL}(l_{HAM} - l^{tar}_{HAM_HFL})$ is the negative length feedback inhibiting the HFL proportional to the stretch of the HAM in the swing phase. In these terms, *G* represents the gain, *l* represents the length of the muscle, and l^{tar} represents the constant target length. Both reflex circuits are active only in the swing phase.
https://doi.org/10.1371/journal.pcbi.1011771.g013

Key reflex circuits for energy-efficient walking over wide range velocity

The aforementioned results suggest that $G_{HFL}(l_{HFL} - l^{tar}_{HFL})$ and $G_{HAM_HFL}(l_{HAM} - l^{tar}_{HAM_HFL})$ could be the parts of the essential reflex circuits on the wide-range velocity walking with maintaining energy efficiency. Therefore, we proceeded to investigate how modulating these reflex circuits affects the energy efficiency of the gait. We measured the change in ∫CoT values when the optimized functions of the control parameters associated with $G_{HFL}(l_{HFL} - l^{tar}_{HFL})$ (reflex circuit 1) and $G_{HAM_HFL}(l_{HAM} - l^{tar}_{HAM_HFL})$ (reflex circuit 2) were replaced with those derived with $A = 10^6$ in the generated gait with $A = 1$ (a baseline), similar to Fig 11, and the result is shown in Fig 14. The cyan and olive bar represents the relative ∫CoT value when we replaced only the optimized functions associated with reflex circuits 1 and 2, respectively. The pink bar represents the relative ∫CoT value when we replaced the optimized function of both reflex circuits. The results indicated that the modulation of only these two reflex circuits resulted in a comparable or even more substantial reduction in ∫CoT value compared to the modulation of all 56 parameters for the case of $A = 10^6$ shown in the purple bar. This finding strongly suggests that the two length-feedback reflex circuits, $G_{HFL}(l_{HFL} - l^{tar}_{HFL})$ and $G_{HAM_HFL}(l_{HAM} - l^{tar}_{HAM_HFL})$, are the key reflex circuits of the energy efficiency in the reflex-based bipedal walking control.

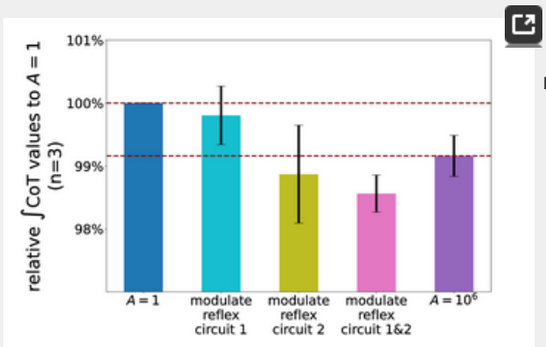

Download:

PPT PowerPoint slide

PNG larger image

TIFF original image

Fig 14. Relative ∫CoT values to the generated walking with *A* = 1 when modulating identified reflex circuits (n = 3).
The cyan and olive bar represents the relative ∫CoT value when only the optimized function of control parameters associated with reflex circuit 1 (i.e. G_{HFL} and l^{tar}_{HFL}) and reflex circuit 2 (i.e. G_{HAM_HFL} and $l^{tar}_{HAM_HFL}$) were replaced with those derived with $A = 10^6$ in the generated gait with $A = 1$, respectively. The pink bar represents when the optimized function of the control parameters associated with both reflex circuits (i.e., G_{HFL}, l^{tar}_{HFL}, G_{HAM_HFL}, $l^{tar}_{HAM_HFL}$) were replaced. The purple bar indicates the value in the generated gait using the optimized functions derived with $A = 10^6$. When circuit 2 was modulated, some generated gaits did not follow the specific input v^{tar}_{vel}, with their velocities being changed by more than 0.05 m/s. Data acquired from the target velocity that resulted in these outliers were excluded from the calculation of estimated CoT curves.
https://doi.org/10.1371/journal.pcbi.1011771.g014

To elucidate the mechanism behind the improved energy efficiency, we examined the change in energy consumption by individual muscles, muscle activation patterns, and stimulation signal for the corresponding muscle when we modulated the two identified reflex circuits. Fig 15 shows the energy consumed by individual muscles during a 30 m walk at $v^{tar}_x = 1.0$. We found that energy consumption of the HFL, GLU, and HAM muscles was significantly reduced after reflex circuits 1 and 2 were modulated. Fig 16 shows the muscle activations of the bipedal model for v^{tar}_x = 1.0 m/s. HFL muscle was mainly activated in the swing phase while GLU and HAM muscles were activated in the stance phase. Fig 17 illustrates the stimulation signal applied to HFL muscle during the swing phase before (blue line) and after the modulation (pink line) of reflex circuits 1 and 2: the stimulation signal applied to HFL muscle decreased after the modulation of these identified reflex circuits.

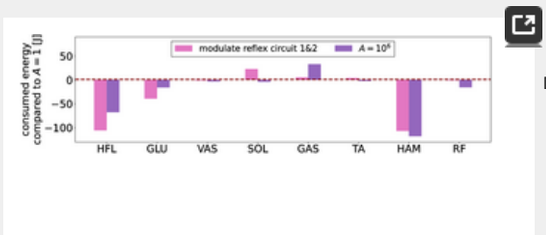

Download:

PPT PowerPoint slide

PNG larger image

TIFF original image

Fig 15. Energy consumed by individual muscles compared to the generated gait with *A* = 1 during a 30 m walk.
v^{tar}_x was set to 1.0 m/s. The pink bars represent the values when the optimized functions of the control parameters associated with reflex circuits 1 and 2 are replaced with those derived with $A = 10^6$ in the gait generated with $A = 1$, and the purple bars represent the values in the gait with $A = 10^6$. The negative value indicates that the energy consumption at the muscle was reduced compared to the generated gait with $A = 1$, while the positive value indicates increased energy consumption.

https://doi.org/10.1371/journal.pcbi.1011771.g015

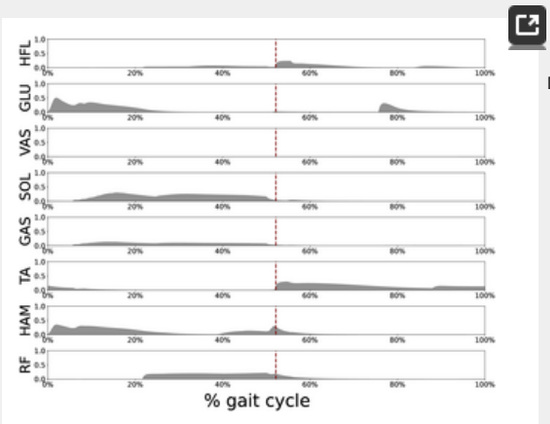

Download:

PPT PowerPoint slide

PNG larger image

TIFF original image

Fig 16. Individual muscle activations.
The gait was generated using the optimized functions derived with $A = 10^6$ and v_x^{tar} was set to 1.0 m/s. The red bar indicates the timing of the transition from stance to swing.
https://doi.org/10.1371/journal.pcbi.1011771.g016

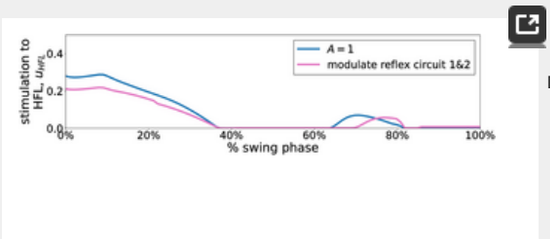

Download:

PPT PowerPoint slide

PNG larger image

TIFF original image

Fig 17. Stimulation to the HFL in the swing phase before and after modulating reflex circuit 1&2.
v_x^{tar} was set to 1.0 m/s. The blue and pink lines are the stimulation to the HFL, which does not drop below 0, at generated gait with $A = 1$ and after the optimized function of the control parameters associated with reflex circuit 1 and 2 are replaced with those derived with $A = 10^6$, respectively.
https://doi.org/10.1371/journal.pcbi.1011771.g017

Robustness to parameter changes

Under various parameter conditions, leg length, sensory time delay, and weight coefficients for the cost function, we have validated the reliability and robustness of the identified two reflex circuits concerning their impact on energy-efficient walking over a wide range of velocities:

- shorten segment length by 20% (different body structure)
- double the time delay of sensory information transmission to the controller (different neural system)
- change the weight coefficients in the objective cost function (Eq (31)), $\alpha_E = 2500$, $\alpha_V = 5$, and $\alpha_t = 0$ (different cost function)

Fig 18 illustrates the relative ∫CoT values to the baseline ($A = 1$) under various conditions. We found that modulating reflex circuits 1 and 2 resulted in decreased ∫CoT values, comparable to the result for all 56 parameter modulation (generated gaits can be seen in S1 Video).

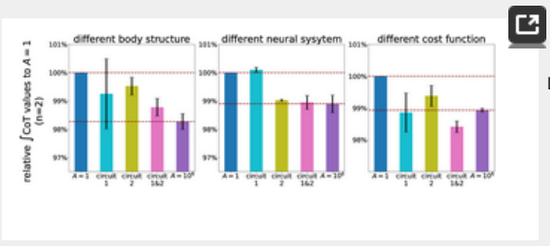

Download:

PPT PowerPoint slide

PNG larger image

TIFF original image

Fig 18. Relative ∫CoT values to the generated walking with $A = 1$ under different setting parameters (n = 2).
In a different body structure setting, the segment lengths of the model were shortened by 20%. In a different neural system setting, the time delay of the sensory information to the controller was doubled. In this setting, stable gaits were not generated for $A > 100$. In a different cost function setting, the weight coefficients in the objective function (Eq (31)) were changed to $\alpha_E = 2500$, $\alpha_V = 5$, and $\alpha_t = 0$.
https://doi.org/10.1371/journal.pcbi.1011771.g018

Discussion

This study aimed to extend the reflex-based control system including velocity control and identify key reflex circuits that play a significant role in energy-efficient walking. We demonstrated that a musculoskeletal model driven by reflex-based control can achieve controlled speeds based on the input target velocity. Subsequently, by utilizing the generated gaits of varying energy efficiencies, we identified two key reflex circuits having a significant impact on CoT values.

We found that the proposed PWLS regression method optimizes the parameter modulator for the reflex-based controller to reproduce more energy-efficient walking across a wide range of velocities. We verified that the ∫CoT values were decreased by giving the bias to the high-performing data in calculating regression curves as shown in Fig 10. These results demonstrate that the PWLS fitting method is more adaptive in evaluating each data point as a weight for performance. However, we also found that the walking generated at an excessively large *A* value resulted in less stability, resulting in a fall at specific target velocities. This can be attributed to insufficiently fast leg swing. Putting the swing leg fast enough in front of the stance leg is essential to prevent falling down [52]. As illustrated in Fig 17, the stimulation applied to the HFL during the swing phase decreased with larger *A*. Consequently, this led to a slow hip flexion resulting in less stability.

As shown in Fig 14, we identified that $G_{HFL}(l_{HFL} - l_{HFL}^{tar})$ and $G_{HAM_HFL}(l_{HAM} - l_{HAM_HFL}^{tar})$ significantly contributed to improve the energy efficiency of the gait generated through reflex-based control. Furthermore, this conclusion has been robustly validated across various settings, including a different body structure, different neural systems, and different cost functions, as shown in Fig 18. Our findings elucidated that the modulation of these reflex circuits resulted in a reduction of stimulation to the HFL during the swing phase, subsequently leading to reduced energy consumption by the HFL, GLU, and HAM (Fig 15). HFL expended less energy due to reduced stimulation. GLU and HAM were mainly activated during the stance phase (Fig 16), and these two muscles are used to maintain the torso balance in the stance phase [28]. Reduced HFL activity during the swing phase leads to less energy consumption at the contralateral GLU and HAM because the work to compensate for torso acceleration caused by HFL is decreased. Therefore, it can be concluded that minimizing the stimulation to the HFL during the swing phase while ensuring sufficient hip swing to prevent falls is essential to improve energy efficiency in reflex-based walking control. This not only reduces HFL activity but also the effort of the GLU and HAM, which compensates for torso acceleration caused by HFL.

The generated walking has several characteristics that demonstrate its biomechanical validity in comparison to the human gait. (i) the *R* values of the hip and knee kinematics were close to 1 ($R > 0.94$ in all cases); (ii) The trajectory of the hip segment height from the ground exhibited a sinusoidal pattern (see Fig. S7 in S1 Appendix) [53]; (iii) we observed both heel strike and toe-off events [54] (see attached movie file); and (iv) a quadratic relationship between walking velocities and CoT [50] (Fig 10). These features are similar to those of human walking from a biomechanical perspective, proving that our simulations do not compromise the dynamically reasonable properties of human walking. Although we agree that reducing the number of control parameters would be essential and helpful for understanding the mechanism underlying walking, we used Wang's extended model rather than Geyer's original model to robustly generate walking without losing biomechanical explanatory ability.

The results of this paper have some limitations concerning similarity to human walking. First, overshoots and undershoots were observed in the measured GRFs (Fig 8) and time evolution of the walking velocities (Fig 9). In the GRF profiles, we found two undershoots in GRF_x and two overshoots in GRF_z. The first occurred at heel strike, and the second occurred at toe-off of the contralateral leg. These overshoots and undershoots can be suppressed by using a lower-impedance ground. However, employing a lower-impedance ground resulted in foot penetration into the ground (refer to S1 Appendix). While the extreme GRF peaks are not biomechanically meaningful, we strongly believe that it is difficult to accurately model contact in a simulation environment [55, 56]. Moreover, we did not observe abrupt or significant changes in joint kinematics attributable to these extreme GRF peaks. Thus, given the difficulty of modeling contact in the simulation environment, the extreme peaks in GRF do not significantly affect kinematics. We conclude that the effects of the extreme peaks of GRF on walking in the musculoskeletal model do not negatively affect the biomechanical meaning of the findings obtained in this study. Second, the cross-correlation values of ankle dorsiflexion were close to 0 compared to hip and knee joints, as shown in Fig 8. At knee joints, the model straightened the knee earlier in the stance phase compared to humans. This strategy is known to generate more efficient solutions in gait optimization [32]. The previous study also showed low cross-correlation values at ankle joints when optimized to minimize energetic cost [32]. Third, we designed the cost function employed in this study to have minimal task terms to generate a human-like gait with more weight on the energy efficiency-related term. This approach optimized the control parameters to improve energy efficiency, consequently allowing the identification of factors that are significant to the energy efficiency of the generated gait over a wide range of walking velocities. More complex cost functions [29, 34, 36] may be required to generate human-like ankle joint kinematics. Finally, although this study successfully demonstrated the implementation of velocity control in a reflex-based control system, it took 20 s to transit walking speed by 1.0 m/s without falling. On the other hand, humans can adjust their walking speed by 1.0 m/s in less than 2 s [57]. Consequently, our control framework lacks the component to change walking speeds rapidly while ensuring stability. Extending the proposed framework is one of the future works to achieve velocity control as fast as humans.

Human locomotion involves complex interactions between descending supraspinal commands, interconnected spinal circuits involving reflexes and CPGs, and the musculoskeletal system. This study primarily focuses on reflexes in the spinal cord. Therefore, we must add other control components for fast walking velocity control. Moreover, we constrained the bipedal model motion into the sagittal plane. Hence, the extension of the motion into three dimensions is another essential future work to apply the controller to engineering applications.

Conclusion

Reflex mechanisms contribute significantly to the generation of stable and energy-efficient walking. However, a major limitation of generating gaits in musculoskeletal models through reflex-based control is the difficulty in precisely regulating velocity due to the large number of control parameters that need to be properly tuned. Extending reflex-based systems to affect velocity controls is essential to explore the reflex modulation mechanism and to understand its energy-efficient maintenance mechanism across a wide range of velocities. Furthermore, the development of energy-efficient control over a wide range of velocities in the reflex-based system will facilitate advanced engineering applications. Therefore, we developed a reflex-based control framework that enables the regulation of walking velocity over a wide range of velocities. Our parameter modulation method using PWLS that calculates the control parameters in response to a target velocity while optimizing efficiency successfully demonstrates generating walking gaits from 0.7 to 1.6 m/s. Furthermore, after a detailed analysis of the parameter modulator in a reflex-based system, we identified that the modulations of two reflex circuits, $G_{HFL}(l_{HFL} - l_{HFL}^{tar})$ and $G_{HAM_HFL}(l_{HAM} - l_{HAM_HFL}^{tar})$, improve energy efficiency of the gait. The coordinated activity in the swing phase between the HFL and HAM reduced the stimulation applied to HFL during the swing phase, which not only caused the reduction of HFL activity but also alleviated the effort of GLU and HAM that compensates for the torso acceleration induced by the HFL. This research will inspire future investigations into reflex mechanisms and facilitate the development of advanced walking control systems for practical applications, such as gait-assisted exoskeletons and prosthetic legs, and robot control.

Supporting information

Detailed description of the main text.
Showing 1/2: pcbi.1011771.s001.zip

- S1_Appendix.pdf
- S1_Fig.tif
- S2_Fig.tif
- S3_Fig.tif
- S4_Fig.tif
- S5_Fig.tif
- S6_Fig.tif
- S7_Fig.tif

figshare _ 1 / 2 Download

S1 Appendix. Detailed description of the main text.
https://doi.org/10.1371/journal.pcbi.1011771.s001
(ZIP)

S1 Video. Video of the generated gait.
https://doi.org/10.1371/journal.pcbi.1011771.s002
(MP4)

References

1. Kandel ER, Schwartz JH, Jessell TM. Principles of neural science. 5th ed. New York: McGraw-Hill; 2013.

2. Sherrington CS. Flexion-reflex of the limb, crossed extension-reflex, and reflex stepping and standing. J Physiol. 1910;40(1)-(2): 28–121. pmid:16993027
View Article • PubMed/NCBI • Google Scholar

3. Eccles JC, Eccles RM, Lundberg A. The convergence of monosynaptic excitatory afferents on to many different species of alpha motoneurons. J Physiol. 1957;137(1): 22–50. pmid:13439582
View Article • PubMed/NCBI • Google Scholar

4. Brown TG. The intrinsic factors in the act of progression in the mammal. Proc R Soc Lond B Biol Sci. 1911;84.
View Article • Google Scholar

5. Grillner S. The motor infrastructure: From ion channels to neuronal networks. Nat Rev Neurosci. 2003;4: 573–586. pmid:12838332
View Article • PubMed/NCBI • Google Scholar

6. Kiehn O. Decoding the organization of spinal circuits that control locomotion. Nat Rev Neurosci. 2016;17: 224–238. pmid:26935168
View Article • PubMed/NCBI • Google Scholar

7. M. Raibert. Legged robots that balance. MIT Press; 1986.

8. Collins SH, Wisse M, Ruina A. A three-dimensional passive-dynamic walking robot with two legs and knees. Int J Robot Res. 2005;20(7).
View Article • Google Scholar

9. Pratt J, Pratt G. Exploiting natural dynamics in the control of a 3D bipedal robot. In Proc CLAWAR. 1999.
View Article • Google Scholar

10. Shahri MA, Mohseni O, Bidgoly HJ, Ahmadabadi MN. Profile Design of Parallel Rotary Compliance for Energy Efficiency in Cyclic Tasks. IEEE/ASME Transactions on Mechatronics. 2020;25(1):142–151.
View Article • Google Scholar

11. Koseki S, Kutsuzawa K, Owaki D, Hayashibe M. Multimodal bipedal locomotion generation with passive dynamics via deep reinforcement learning. Front Neurorobot. 2023; 16:1054239. pmid:36756534
View Article • PubMed/NCBI • Google Scholar

12. Hara H, Sankai Y. Development of HAL for lumbar support. In Proc SCIS & ISIS. 2010.
View Article • Google Scholar

13. Baud R, Manzoori AR, Ijspeert A, Bouri M. Review of control strategies for lower-limb exoskeletons to assist gait. J Neuro Engineer Rehab. 2021;18(119). pmid:34315499
View Article • PubMed/NCBI • Google Scholar

14. Siviy C, Baker LM, Quinlivan BT, Porciuncula F, Swaminathan K, Awad LN, et al. Opportunities and challenges in the development of exoskeletons for locomotor assistance. Nat Biomed Eng. 2022. pmid:36550303
View Article • PubMed/NCBI • Google Scholar

15. Firouzi V, Mohseni O, Sharbafi MA. Model-based Control for Gait Assistance in the Frontal Plane. IEEE RAS/EMBS International Conference for Biomedical Robotics and Biomechatronics. 2022: 1–8.

16. Elery T, Rezazadeh S, Nesler C, Gregg RD. Design and validation of a powered knee–ankle prosthesis with high-torque, low-impedance actuators. IEEE Trans Robotics. 2020;36(6): 1649–1668. pmid:33299386
View Article • PubMed/NCBI • Google Scholar

17. Eilenberg MF, Geyer H, Herr H. Control of a powered ankle–foot prosthesis based on a neuromuscular model. IEEE Trans Neural Sys Rehab Engin. 2010;18(2): 164–173. pmid:20071268
View Article • PubMed/NCBI • Google Scholar

18. Obuchi SP, Kawai H, Murakawa K. Reference value on daily living walking parameters among Japanese adults. Geriatr Gerontol Int. 2020;20(7):664–669. pmid:32378318
View Article • PubMed/NCBI • Google Scholar

19. Duysens J, Clarac F, Cruse H. Load-regulating mechanisms in gait and posture: Comparative aspects. Physiol Rev. 2000;80(1): 83–133. pmid:10617766
View Article • PubMed/NCBI • Google Scholar

20. Pearson KG. Generating the walking gait: Role of sensory feedback. Progress Brain Res. 2004;143: 123–129. pmid:14653157
View Article • PubMed/NCBI • Google Scholar

21. Rossignol S, Dubuc R, Gossard JP. Dynamic sensorimotor interactions in locomotion. Physiol Rev. 2006;86(1): 89–154. pmid:16371596
View Article • PubMed/NCBI • Google Scholar

22. Grillner S, Wallen P, Saitoh K, Kozlov A, Robertson B. Neural bases of goal-directed locomotion in vertebrates–An overview. Brain Res Rev. 2008;57(1): 2–12. pmid:17916382
View Article • PubMed/NCBI • Google Scholar

23. McCrea DA, Rybak IA. Organization of mammalian locomotor rhythm and pattern generation. Brain Res Rev. 2008;57(1): 134–146. pmid:17936363
View Article • PubMed/NCBI • Google Scholar

24. Lam T, Pearson KG. The role of proprioceptive feedback in the regulation and adaptation of locomotor activity. Sensorimotor control of movement and posture. 2002: 343–355. pmid:12171130
View Article • PubMed/NCBI • Google Scholar

25. Zehr EP, Stein RB. What functions do reflexes serve during human locomotion? Prog Neurobiol. 1999;58(2): 185–205. pmid:10338359
View Article • PubMed/NCBI • Google Scholar

26. Petersen NT, Morita H, Nielsen J. Modulation of reciprocal inhibition between ankle extensors and flexors during walking in man. J Physiol. 1999;520(2): 605–619. pmid:10523426
View Article • PubMed/NCBI • Google Scholar

27. De Groote F, Falisse A. Perspective on musculoskeletal modeling and predictive simulations of human movement to assess the neuromechanics of gait. In Proc Royal Soc B. 2021;288(1946): 20202432. pmid:33653141
View Article • PubMed/NCBI • Google Scholar

28. Geyer H, Herr H. A muscle-reflex model that encodes the principles of legged mechanics produces human walking dynamics and muscle activity. IEEE Trans Neural Sys Rehab Engin. 2010;18(3): 263–273.
View Article • Google Scholar

29. Wang JM, Hamner SR, Delp SL, Koltun V. Optimizing locomotion controllers using biologically based actuators and objectives. ACM TOG. 2012;31(4): 1–11. pmid:26251560
View Article • PubMed/NCBI • Google Scholar

30. Song S, Geyer H. Regulating speed and generating large-speed transitions in a neuromuscular human walking model. In Proc IEEE Int Conf Robot Automat. 2012: 511–516.

31. Song S, Geyer H. Generalization of a muscle-reflex control model for 3D walking. In Proc Int Conf IEEE Engin Med Biol Soc. 2013;2013: 7463–7466. pmid:24111471
View Article • PubMed/NCBI • Google Scholar

32. Song S, Geyer H. Neural circuitry that emphasizes spinal feedback generates diverse behaviors in human locomotion. J Physiol. 2015;593(16): 3493–3511.
View Article • Google Scholar

33. Wang J, Qin W, Sun L. Terrain adaptive walking of biped neuromuscular virtual human using deep reinforcement learning. IEEE Access. 2019;7: 92465–92475.
View Article • Google Scholar

34. Ong CF, Geijtenbeek T, Hicks JL, Delp SL. Predicting gait adaptations due to ankle plantarflexor muscle weakness and contracture using physics-based musculoskeletal simulations. PLoS Comput Biol. 2019;15(10): e1006993. pmid:31589597
View Article • PubMed/NCBI • Google Scholar

35. Davoodi A, Mohseni O, Seyfarth A, Sharbafi MA. From template to anchors: transfer of virtual pendulum posture control balance template to adaptive neuromuscular gait model increases walking stability. R Soc Open Sci. 2019;6(3):181911. pmid:31032044
View Article • PubMed/NCBI • Google Scholar

36. Di Russo A, Stanev D, Armand S, Ijspeert A. Sensory modulation of gait characteristics in human locomotion: A neuromusculoskeletal modeling study. PLOS Comput Biol. 2021;17(5): e1008594. pmid:34010288
View Article • PubMed/NCBI • Google Scholar

37. Ramadan R, Geyer H, Jeka J, Schöner G, Reimann H. A neuromuscular model of human locomotion combines spinal reflex circuits with voluntary movement. Scientif Rep. 2022;12(1): 1–23.
View Article • Google Scholar

38. Dzeladini F, Van Den Kieboom J, Ijspeert A. Contribution of central pattern generator to reflex-based neuromuscular model. Front Human Neurosci. 2014;8: 371.
View Article • Google Scholar

39. Tamburella F, Tagliamonte NL, Pisotta I, Masciullo M, Arquilla M, van Asseldonk EHF, van der Kooij H, Wu AR, Dzeladini F, Ijspeert AJ, Molinari M. Neuromuscular Controller Embedded in a Powered Ankle Exoskeleton: Effects on Gait, Clinical Features and Subjective Perspective of Incomplete Spinal Cord Injured Subjects. IEEE Trans Neural Syst Rehabil Eng. 2020;28(5):1157–1167. pmid:32248116
View Article • PubMed/NCBI • Google Scholar

40. Wu AR, Dzeladini F, Brug TJ, Tamburella F, Tagliamonte NL, Van Asseldonk EH, et al. An adaptive neuromuscular controller for assistive lower-limb exoskeletons: A preliminary study on subjects with spinal cord injury. Front Neurorobot. 2017;11: 30.
View Article • Google Scholar

41. Thatte N, Geyer H. Toward Balance Recovery With Leg Prostheses Using Neuromuscular Model Control. IEEE Trans Biomed Engin. 2016;63(5): 904–913. pmid:26315935
View Article • PubMed/NCBI • Google Scholar

42. Todorov E, Erez T, Tassa Y. MuJoCo: A physics engine for model-based control. In Proc IEEE/RSJ Int Conf Intell Robot Sys. 2012: 5026–5033.
View Article • Google Scholar

43. Ikkala A, Hämäläinen P. Converting Biomechanical Models from OpenSim to MuJoCo. Converging Clinical and Engineering Research on Neurorehabilitation IV. 2021: 277–281.

44. Wang H, Caggiano V, Durandau G, Sartori M, Kumar V. MyoSim: Fast and physiologically realistic MuJoCo models for musculoskeletal and exoskeletal studies. International Conference on Robotics and Automation. 2022: 8104–8111.

45. DeepMind Technologies Limited. MuJoCo Modeling–Muscle Actuators. n.d. Available from https://mujoco.readthedocs.io/en/latest/modeling.html#cmuscle.

46. Hansen N. CMA evolution strategy: A comparative review. Towards a new evolutionary computation. Advances in the estimation of distribution algorithms; 2006. pp. 75–102.

47. Ruina A, Bertram JE, Srinivasan M. A collisional model of the energetic cost of support work qualitatively explains leg sequencing in walking and galloping, pseudo-elastic leg behavior during running, and walk-to-run transition. J Theoretic Biol. 2005;237(2): 170–192. pmid:15961114
View Article • PubMed/NCBI • Google Scholar

48. Anderson III FC. Dynamic optimization solution for a complete cycle of normal gait. University of Texas at Austin; 1999.

49. Cleveland WS and Devlin SJ. Locally weighted regression: an approach to regression analysis by local fitting. JASA. 1988;83(403): 596–610.
View Article • Google Scholar

50. Carrier DR, Kapoor A, Kimura T, Nickels MK, Satwanti , Scott EC, et al. The energetic paradox of human running and hominid evolution [comments and replies]. Curr Anthropol. 1984;25(4): 483–495.
View Article • Google Scholar

51. Schwartz MH, Rozumalski A, Trost JP. The effect of walking speed on the gait of typically developing children. J Biomech. 2008;41(8):1639–50. pmid:18466909
View Article • PubMed/NCBI • Google Scholar

52. Wisse M, Schwab AL, van der Linde RQ, van der Helm FCT. How to keep from falling forward: elementary swing leg action for passive dynamic walkers. IEEE Transactions on Robotics. 2005;21(3):393–401.
View Article • Google Scholar

53. Cavagna GA, Thys H, Zamboni A. The sources of external work in level walking and running. J Physiol. 1976;262(3):639–57. pmid:1011078
View Article • PubMed/NCBI • Google Scholar

54. Usherwood JR, Channon AJ, Myatt JP, Rankin JW, Hubel TY. The human foot and heel–sole–toe walking strategy: a mechanism enabling an inverted pendular gait with low isometric muscle force?. Journal of The Royal Society Interface. 2012;9(75):2396–2402. pmid:22572024
View Article • PubMed/NCBI • Google Scholar

55. Todorov E. Convex and analytically-invertible dynamics with contacts and constraints: Theory and implementation in MuJoCo. IEEE International Conference on Robotics and Automation. 2014:6054–6061.

56. Castro AM, Permenter FN, Han X. An unconstrained convex formulation of compliant contact. IEEE Transactions on Robotics. 2022:1301–1320.
View Article • Google Scholar

57. Boripuntakul S, Kamnardsiri T, Lord SR, Maiarin S, Worakul P, Sungkarat S. Gait variability during abrupt slow and fast speed transitions in older adults with mild cognitive impairment. PLoS One. 2022;17(10). pmid:36269750
View Article • PubMed/NCBI • Google Scholar

Publications

PLOS Biology
PLOS Climate
PLOS Complex Systems
PLOS Computational Biology
PLOS Digital Health
PLOS Genetics
PLOS Global Public Health
PLOS Medicine
PLOS Mental Health
PLOS Neglected Tropical Diseases
PLOS ONE
PLOS Pathogens
PLOS Sustainability and Transformation
PLOS Water

Home
Blogs
Collections
Give feedback
LOCKSS

Privacy Policy
Terms of Use
Advertise
Media Inquiries
Contact

PLOS is a nonprofit 501(c)(3) corporation, #C2354500, based in San Francisco, California, US